

# Dynamic modeling and control of a novel XY positioning stage for semiconductor packaging

Fujun Wang<sup>1,2</sup>, Zhipeng Ma<sup>1</sup>, Weiguo Gao<sup>1</sup>, Xingyu Zhao<sup>1</sup>, Yanling Tian<sup>1</sup>, Dawei Zhang<sup>1</sup> and Cunman Liang<sup>1</sup>

Transactions of the Institute of  
Measurement and Control  
1–13

© The Author(s) 2014

Reprints and permissions:

sagepub.co.uk/journalsPermissions.nav

DOI: 10.1177/0142331214541598

tim.sagepub.com



## Abstract

This paper presents the dynamic modeling and controller design of an XY positioning stage for semiconductor packaging. The XY stage is directly driven by two linear voice coil motors, and motion decoupling between the X and Y axes is realized through a novel flexible decoupling mechanism based on flexure hinges and preloaded spring. Through bond graph method, the dynamic models of X- and Y-axes servomechanisms are established, respectively, and the state space equations are derived. A control methodology is proposed based on force compensations and the performance of the XY stage is investigated by simulations and experimental tests. The results show that the XY stage has good performance. When the reference displacements are defined as 2 mm, the settling time of the X-axis movement is 64 ms, and the overshoot is 0.7%. Y-axis settling time is 62 ms, and the overshoot is 0.8%. X-axis positioning accuracy is 1.85  $\mu\text{m}$  and the repeatability is 0.95  $\mu\text{m}$ . Y-axis positioning accuracy and repeatability are 1.75  $\mu\text{m}$  and 0.9  $\mu\text{m}$ , respectively. In addition, the stage can track linear, circular and complex trajectories very well.

## Keywords

XY positioning stage, dynamic modeling, control

## Introduction

Recently, the trend towards miniaturizing semiconductor products such as integrated chips and MEMS has stimulated extensive research on semiconductor packaging (Aized and Shirinzadeh, 2011; Fatikow et al., 2008; Li and Xu, 2011; Liaw et al. 2008; Wang et al., 2009b; Zhang et al., 2013). As one of the essential components of semiconductor packaging machines, high speed XY positioning stage with a micro scale resolution and motion stroke of over several millimeters plays an important role in the packaging process (Hwang et al., 2010; Liang et al., 2010; Wang et al., 2011, 2014).

Numerous new drive technologies (e.g., piezoelectric, electrostatic, etc.) have been utilized in the XY positioning stages (Li and Xu, 2011; Tian et al., 2009). However, electromagnetic actuation is still considered to be the best choice for the motion with a long stroke of more than several millimeters (Khan et al., 2011). Most traditional XY stages equipped with rotational motors and ball screws have disadvantages of reduced accuracy, complex mechanical structure and low reliability, and it can not meet the stringent requirements of precision manufacturing and assembly industry (Hace et al., 2011; Liu et al., 2003). Direct-drive motors have the advantages of low friction and high mechanical stiffness, and thus they have been increasingly used in the high speed precision positioning XY stage (Dejima et al., 2005; Sanchez-Salmeron and Ricolfe-Viala, 2012). Consequently, it is very essential to study on the dynamic modeling and controller design of the

direct-drive stage to cope with the increasingly demanding requirements.

Dynamic model is the basic of dynamic analysis and controller design, so many researchers have been working on the dynamic modeling and analysis of XY stages. Teo et al. (2007) and Zhao et al. (2010) established the dynamic models of the mechanical system of an H-type gantry direct-drive stages using Lagrangian equation. Cai et al. (2011) carried out the dynamic modeling of a 3-DOF ultra-precision positioning stage with air bearing through rigid body finite rotation Jourdain Principle and the vibration frequency and mode were analysed and discussed. A numerical method based on mechanical energy conservation was adopted to calculate the undamped natural frequency of a parallel-kinematic positioning XY stage (Ferreira et al., 2007). Fung et al. (2009) achieved the dynamic model of a dual-stage XY precision-positioning table with the aid of analytical method and

<sup>1</sup>Tianjin Key Laboratory of Equipment Design and Manufacturing Technology, School of Mechanical Engineering, Tianjin University, Tianjin, China

<sup>2</sup>Department of Mechanical Science and Engineering, University of Illinois at Urbana-Champaign, Urbana, USA

## Corresponding author:

Weiguo Gao, Tianjin Key Laboratory of Equipment Design and Manufacturing Technology, School of Mechanical Engineering, Tianjin University, 92 Weijin Road, Nankai District, Tianjin 300072, China.  
Email: gaowg@tju.edu.cn

experimental identification approach. The high-speed precision-positioning  $XY$  stage is a complex system which integrates mechanical, electrical and other physical processes. During the high-speed motion with short strokes, the  $XY$  stage usually shows the characteristics of high-order, multi-variable and time-varying, so the dynamic behavior of the  $XY$  stage becomes extremely complex. The dynamic model obtained through the above traditional theoretical modeling methods can not accurately demonstrate the actual dynamic behavior of such complex systems. As a global dynamic modeling method, bond graph represents the system in terms of energy and information flow, and the advantage of this method is that the dynamic model in multi-energy domains can be constructed in a rather small set of ideal elements (Sun et al., 2011; Wang et al., 2009b). As a result, it is very suitable for the dynamic modeling and characteristic analysis of high-speed and high-accuracy positioning  $XY$  stage.

The controller is one of the important elements of an  $XY$  positioning stage, because of its ability to eliminate positioning errors. In the literature, proportion-integration-differentiation (PID) compensator is by far the most widely used form of feedback controller (Ang et al., 2005). However, it cannot meet the increasingly stringent performance requirements of the high-speed  $XY$  positioning stage (Liu et al. 2005). Wang et al. (2006) presented a combination of friction compensator and disturbance observer (DOB) to eliminate the uncompensated friction and other external disturbances for a direct-drive stage. Tomizuka (1987) proposed a zero phase error tracking controller (ZPETC) based on approximate inversion of the closed-loop system to eliminate time delay disturbance and improve tracking performance of an  $XY$  stage. Several advanced control theories including the adaptive robust control (ARC) (Xu and Yao, 2000), variable-structure control (VSC) (Adamy and Flemming, 2004), iterative learning control (Wu and Ding, 2007), fuzzy control (Mou and Sung, 2012) and neural networks control (Xu and Li, 2012), were proposed to control direct-drive positioning stages, and they can provide appropriate level of

performance. However, their applications are limited in industry applications by the expensive algorithms and calculations. In addition, these studies mostly focused on linear motor direct-drive  $XY$  stages.

In this paper, the dynamic modeling and controller design of a precision positioning  $XY$  stage for semiconductor packaging are presented. Firstly we describe the configuration of the  $XY$  stage with a novel decoupling mechanism. Then, considering the characteristics of the servomechanism, the dynamic model is established using bond graph method. On the basis of force compensation principle, the controller is designed. Finally, the performance of the  $XY$  stage is evaluated by simulations and experimental tests.

## Dynamic modeling of the $XY$ stage

Prior to the modeling of the  $XY$  positioning stage, a brief description of the mechanism of the  $XY$  stage will provide a good basis for the subsequent discussion.

### Mechanical structure

The mechanism of the linear voice coil motors (LVCMS) direct-drive  $XY$  stage is shown in Figure 1. The stage is mainly composed of  $X$ - and  $Y$ -axes LVCMS,  $X$ - and  $Y$ -axes tables, the motion decoupling mechanism and the base. Linear grating encoders are used as the feedback sensors for  $X$ - and  $Y$ -axes tables. The  $X$ - and  $Y$ -axes motors are both fixed on the base. The  $X$ -axis table is connected with  $X$ -axis LVCMS by the pushing plate. The  $Y$ -axis table is located above  $X$ -axis table, and it is also connected to the  $Y$ -axis LVCMS by the motion decoupling mechanism. The  $Y$ -axis motor is connected to the guiding fin which can move in  $Y$  axis on the sliding guides. One end of the preloaded connecting rod is mounted on the guiding fin and the other end is connected to the preload spring. The preload spring is also mounted on the guiding fin. The front and back roller bearings are mounted on the guiding fin and roll contact the front and back lapping plates, respectively.

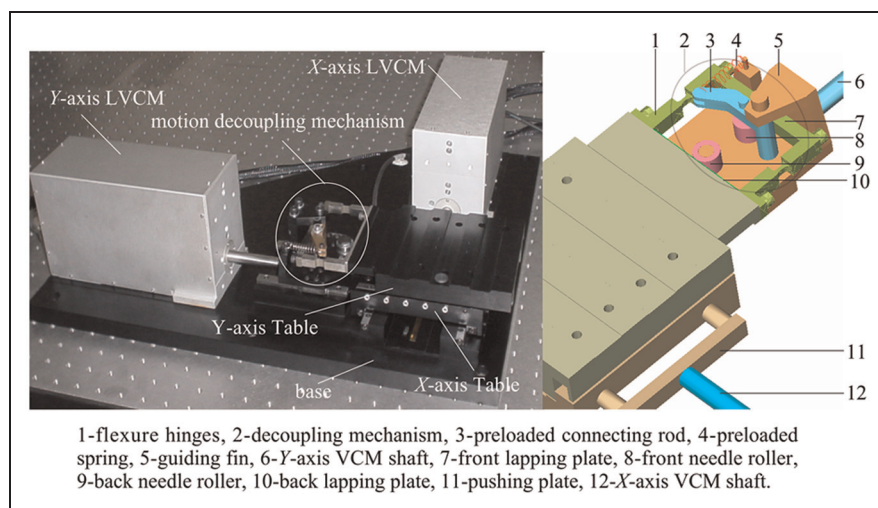
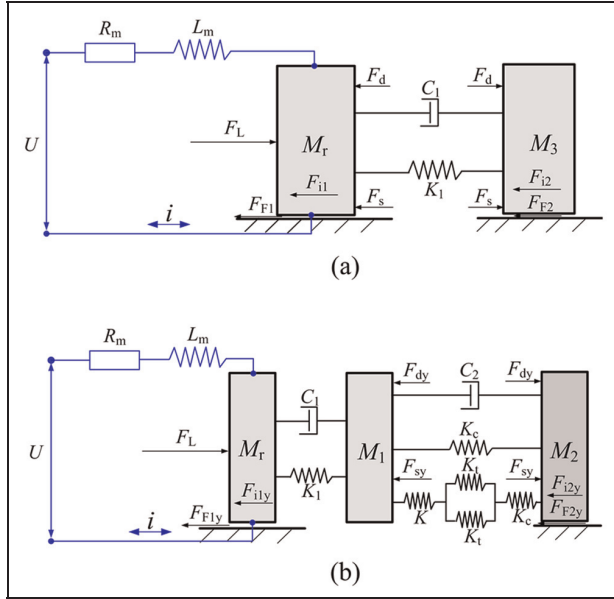


Figure 1. The configuration of the LVCMS direct-drive  $XY$  stage.



**Figure 2.** The dynamic model of the LVCMs direct-drive XY stage: (a) for the X axis, and (b) for the Yaxis.

The decoupling mechanism is composed of the guiding fin, preloaded connecting rod, back roller bearing, front roller bearing, back lapping plate, front lapping plate, flexure hinges and the preloaded spring. The Y-axis LVCM is connected to the guiding fin which can move in Y axis on the sliding guides. One end of the preloaded connecting rod is mounted on the guiding fin and the other end is connected to the preload spring. The preload spring is also mounted on the guiding fin. The front and back roller bearings are mounted on the guiding fin and roll contact with the front and back lapping plates, respectively.

The Y-axis motor generates a force, which will drive the Y-axis table by the flexible decoupling mechanism. When X-axis motor generates a force, the Y-axis table will move with X-axis table in X direction, the front and back roller bearings roll along the front and back lapping plate separately, and thus the motion decoupling of X- and Y- axes is realized. Thus the motion mass can be greatly reduced. Moreover, the dynamic load and the residual vibrations during high speed motion and the instant interference generated when X- and Y-axes motion at the same time can be suppressed by the slight deformation of flexure hinges.

### Dynamic modeling using bond graph method

The dynamic model of the VCMs direct-drive XY stage is shown in Figure 2, where  $U$  is the voltage applied to the VCM,  $R_m$  is the resistance of the VCM coil,  $i$  is the current intensity through the coil,  $L_m$  is the inductance of the VCM coil,  $M_r$  is the mass of the coil,  $M_1$  and  $M_2$  are the equivalent mass of the Y-axis guiding fin and table, respectively,  $M_3$  is the mass of the X-axis table,  $K_1$  and  $C_1$  are the connecting stiffness and damping between coil and the guiding fin, respectively,  $K$  is the stiffness of the preload spring,  $K_t$  is the stiffness of the flexure hinge,  $K_c$  is the contact stiffness

between the bearing and the lapping plate,  $C_2$  is the equivalent damping between the Y-axis guiding fin and table,  $F_L$  is the output force of the coil,  $F_d$  is the X-axis damping force,  $F_s$  is the X-axis equivalent spring force,  $F_{dy}$  is the Y-axis damping force,  $F_{sy}$  is the Y-axis equivalent spring force,  $F_{F1}$  is the friction of the X-axis coil,  $F_{F2}$  is the friction of the X-axis table,  $F_{F1y}$  is the friction of the Y-axis coil,  $F_{F2y}$  is the friction of the Y-axis table,  $F_{i1}$  is the inertia force of the X-axis coil,  $F_{i2}$  is the inertia force of the X-axis table,  $F_{i1y}$  is the inertia force of the Y-axis coil, and  $F_{i2y}$  is the inertia force of the Y-axis table.

A VCM is basically an electromagnetic transducer in which a coil is placed in a magnetic pole gap experiences a force proportional to the current passing through the coil. Assuming that the force generated by the VCM is independent of the position, the governing equations can be written as equations (1) and (2)

$$U = R_m i + L_m \frac{di}{dt} + K_B v \quad (1)$$

$$F = K_F i = M_r \frac{dv}{dt} + F_L \quad (2)$$

where  $v$  is the motion velocity of the VCM coil,  $F$  is the force generated by the VCM,  $K_B$  is the coefficient of induced electromotive force, and  $K_F$  is the force coefficient.

The dynamics of the X- and Y-axes servomechanism is represented by the following second-order linear differential equations.

$$M_3 \frac{d^2 x}{dt^2} + C_1 \frac{dx}{dt} + K_1 x = F_L - F_{F2} \quad (3)$$

$$M_y \frac{d^2 y}{dt^2} + C_y \frac{dy}{dt} + K_y y = F_y \quad (4)$$

where  $x$  is the displacement of X-axis table,  $M_y = \begin{bmatrix} M_1 & 0 \\ 0 & M_2 \end{bmatrix}$ ,  $C_y = \begin{bmatrix} C_1 + C_2 & -C_2 \\ -C_2 & C_2 \end{bmatrix}$ ,  $K_y = \begin{bmatrix} K_1 + K_{y2} & -K_{y2} \\ -K_{y2} & K_{y2} \end{bmatrix}$ ,  $y = \begin{bmatrix} y_1 \\ y_2 \end{bmatrix}$ ,  $F_y = \begin{bmatrix} F_L \\ -F_{F2} \end{bmatrix}$ ,  $K_{y2} = \frac{2K_t K_c}{2K_t K_c + 2K_t K_c + K K_c} + K_c$ ,  $y_1$  and  $y_2$  are the displacements of Y-axis guiding fin and table, respectively.

Exponential friction model is adopted, and it can be expressed as

$$F_F(v_f) = \text{signum}(v_f) \cdot (F_c + (F_{st} - F_c) \cdot e^{-\frac{|v_f|}{v_s}}) + \mu v_f \quad (5)$$

where  $v_f$  is velocity,  $F_c$  is coulomb friction,  $F_{st}$  is static friction,  $v_s$  is Stribeck velocity, and  $\mu$  is viscous friction coefficient.

Bond graph is an explicit graphical tool for capturing the common energy structure of systems, and by this approach, a physical system can be represented by symbols and lines, identifying the power flow paths. The basic variables in bond graph are effort ( $e$ ), flow ( $f$ ), time integral of effort ( $p(t)$ ) and the time integral of flow ( $q(t)$ ). Based on the principle of bond graph method, the output force of VCM is defined as the effort source ( $\mathcal{S}_e$ ), the connecting damping and friction are defined as resistor elements ( $\mathcal{R}$ ), and the connecting stiffness is defined as capacitor element ( $\mathcal{C}$ ). Thus the bond graph

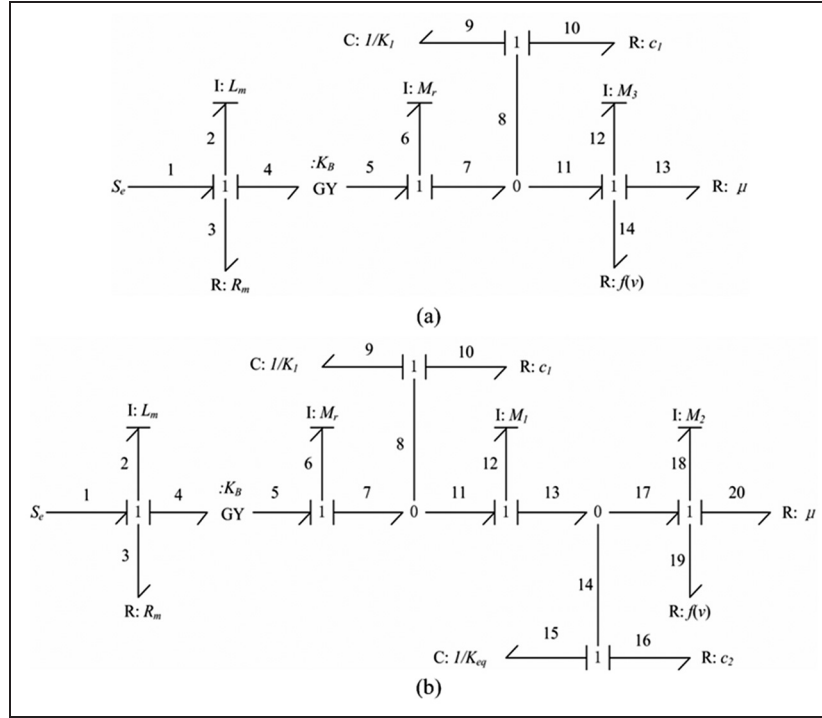


**Figure 3.** The bond graph of the LVCMs direct-drive XY stage: (a) for the X axis, and (b) for the Yaxis.

for X- and Y-axes servomechanism can be obtained, and they are described in Figure 3(a) and Figure 3(b), respectively.

In the Y-axis bond graph, according to the 1-junction that connects the bonds of 8, 9 and 10, the following equation can be gotten.

$$F_L = K_1 q_9 + C_1 v_{10} \quad (6)$$

Considering the 0-junction that connects the bonds of 7, 8 and 11, the following equation can be obtained.

$$v_{10} = v_r - v_1 = v_r - \frac{dy_1}{dt} \quad (7)$$

Considering the 0-junction that connects the bonds of 13, 14 and 17, the following equation can be gotten.

$$v_{16} = v_1 - v_2 = \frac{dy_1}{dt} - \frac{dy_2}{dt} \quad (8)$$

Considering the 1-junction that connects the bonds of 11, 12 and 13 and the 1-junction that connects the bonds of 17, 18 and 19, the following equation can be achieved.

$$F_L = M_1 a_{12} + M_2 a_{18} + f(v_{19}) + \mu v_{19} \quad (9)$$

And

$$f(v_{19}) = \text{signum}(v_{19})(F_c + (F_{st} - F_c)e^{-\frac{|v_{19}|}{v_s}}) \quad (10)$$

According to the 1-junction that connects the bonds of 14, 15 and 16, the following equation can be gotten.

$$F_L - M_1 a_{12} = K_{eq} q_{15} + C_2 v_{16} \quad (11)$$

$$\text{where } K_{eq} = K_c + \frac{2K_t K K_c}{2K_t + K + K_c}$$

Considering the inertia and capacitance effects have great significances to the dynamic performance of the system, the generalized momentum  $p(t)$  of inertia element and generalized displacement  $q(t)$  are selected as the state variables of the XY stage.

X-axis state variables can be expressed as

$$\mathbf{x}_x = [p_2 \ p_6 \ q_9 \ p_{12}]^T = [f_2 L_m \ f_6 M_r \ \frac{e_9}{K_1} \ f_{12} M_3]^T \quad (12)$$

The input variable  $\mathbf{u}_x = [e_1]$ , and the output variable is  $\mathbf{y}_x = [f_{12}]$ . According to the relation of the power flow and the definition of basic elements, the X-axis state space equation and output equation can be gotten, and they are written as

$$\dot{\mathbf{x}}_x = \mathbf{A}_x \mathbf{x}_x + \mathbf{B}_x \mathbf{u}_x \quad (13)$$

$$\mathbf{y}_x = \mathbf{C}_x \mathbf{x}_x + \mathbf{D}_x \mathbf{u}_x \quad (14)$$

$$\text{where } \mathbf{A}_x = \begin{bmatrix} -\frac{R_m}{L_m} & -\frac{K_B}{M_r} & 0 & 0 \\ \frac{K_B}{L_m} & -\frac{C_1}{M_r} & -K_1 & 0 \\ 0 & \frac{1}{M_r} & 0 & -\frac{1}{M_3} \\ 0 & \frac{C_1}{M_r} & 0 & -\frac{C_1 + \mu}{M_3} \end{bmatrix}, \mathbf{B}_x = \begin{bmatrix} 1 \\ 0 \\ 0 \\ 0 \end{bmatrix},$$

$$\mathbf{C}_x = \begin{bmatrix} 0 & 0 & 0 & 0 \end{bmatrix} \frac{1}{M_3}, \text{ and } \mathbf{D}_x = 0.$$

Y-axis state variables can be expressed as

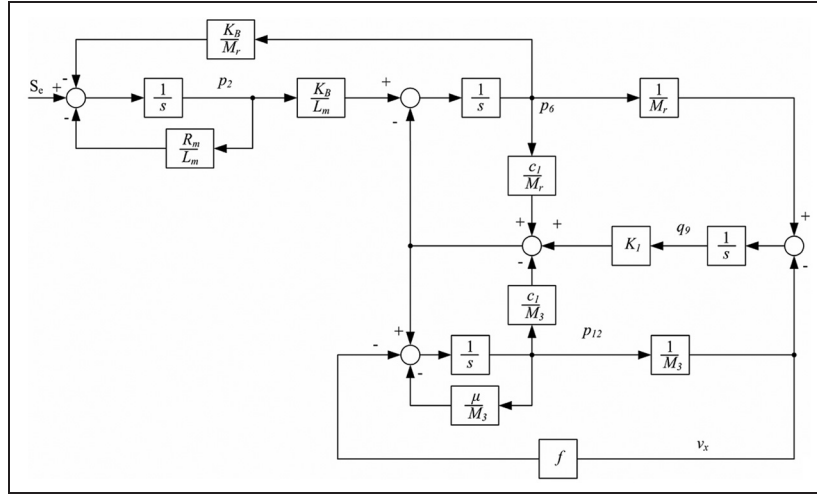


**Figure 4.** The global system control diagram for the X-axis servomechanism.

$$\begin{aligned} \mathbf{x}_y &= [p_2 \quad p_6 \quad q_9 \quad p_{12} \quad q_{15} \quad p_{18}]^T \\ &= [f_2 L_m \quad f_6 M_r \quad \frac{e_9}{K_1} \quad f_{12} M_1 \quad \frac{e_{15}}{K_{eq}} \quad f_{18} M_2]^T \end{aligned} \quad (15)$$

The input variable  $\mathbf{u}_y = [e_1]$ , and the output variable is  $\mathbf{y}_y = [f_{12}]$ . The relation between the effort and flow variables of resistor elements in the Y-axis bond graph can be described by

$$\begin{aligned} \mathbf{e} &= [e_3 \quad e_{10} \quad e_{16} \quad e_{19} \quad e_{20}]^T \\ &= [f_3 R_m \quad f_{10} C_1 \quad f_{16} C_2 \quad f(f_{12}) \quad \mu f_{20}]^T \end{aligned} \quad (16)$$

Based on the integral causal relations of the basic elements in the Y-axis bond graph, the following equation can be obtained.

$$\begin{aligned} \dot{\mathbf{x}}_y &= [\dot{p}_2 \quad \dot{p}_6 \quad \dot{q}_9 \quad \dot{p}_{12} \quad \dot{q}_{15} \quad \dot{p}_{18}]^T \\ &= [e_2 \quad e_6 \quad f_9 \quad e_{12} \quad f_{15} \quad e_{18}]^T \end{aligned} \quad (17)$$

According to the relation of the power flow and the definition of basic elements, the Y-axis state space equation and output equation can be achieved, and they are written as

$$\dot{\mathbf{x}}_y = \mathbf{A}_y \mathbf{x}_y + \mathbf{B}_y \mathbf{u}_y \quad (18)$$

$$\mathbf{y}_y = \mathbf{C}_y \mathbf{x}_y + \mathbf{D}_y \mathbf{u}_y \quad (19)$$

where

$$\mathbf{A}_y = \begin{bmatrix} -\frac{R_m}{L_m} & -\frac{K_B}{M_r} & 0 & 0 & 0 & 0 \\ \frac{K_B}{L_m} & -\frac{C_1}{M_r} & -K_1 & \frac{C_1}{M_1} & 0 & 0 \\ 0 & \frac{1}{M_r} & 0 & -\frac{1}{M_1} & 0 & 0 \\ 0 & \frac{C_1}{M_r} & K_1 & -\frac{C_1 + C_2}{M_1} & -K_{eq} & \frac{C_2}{M_2} \\ 0 & 0 & 0 & \frac{1}{M_1} & 0 & -\frac{1}{M_2} \\ 0 & 0 & 0 & \frac{C_2}{M_1} & K_{eq} & -\frac{C_2 + \mu}{M_1} \end{bmatrix},$$

$$\mathbf{B}_y = \begin{bmatrix} 1 \\ 0 \\ 0 \\ 0 \\ 0 \\ 0 \end{bmatrix}, \mathbf{C}_y = \begin{bmatrix} 0 & 0 & 0 & 0 & 0 & \frac{1}{M_2} \end{bmatrix}, \text{ and } \mathbf{D}_y = 0.$$

Thus the global system control diagrams for X- and Y-axes servomechanisms can be established, and they are depicted in Figure 4 and Figure 5, respectively. Figure 6 displays the diagram for the Y-axis nonlinear friction. The related system parameters are shown as follows:  $R_m = 16 \, \Omega$ ,  $L_m = 0.027 \, \text{H}$ ,  $K_F = 86 \, \text{N/A}$ ,  $K_B = 116.6 \, \text{N/A}$ ,  $M_1 = 1.205 \, \text{kg}$ ,  $M_2 = 1.2 \, \text{kg}$ ,  $M_3 = 4.006 \, \text{kg}$ ,  $C_1 = 110 \, \text{N}\cdot\text{s/m}$ ,  $C_2 = 110 \, \text{N}\cdot\text{s/m}$ ,  $K_1 = 2.6 \times 10^7 \, \text{N/m}$ ,  $K_{eq} = 1.2 \times 10^5 \, \text{N/m}$ ,  $F_c = 11 \, \text{N}$ ,  $F_{st} = 9 \, \text{N}$ ,  $v_s = 0.004 \, \text{m/s}$ , and  $\mu = 120 \, \text{N}\cdot\text{s/m}$ .

## Controller design

A model-based control methodology is presented to control the XY stage. In order to reduce the deviations of displacement, velocity and acceleration in terms of force compensation, the controller is realized through transforming the forces applied to the VCM coil and tables to the control voltage signals. The cascaded control structure including three closed-loops is adopted. For X-axis servomechanism, the PWM servo driver is used, and its transfer function is given as follow

$$G_{PWM}(s) = K_s / (T_s s + 1) \quad (20)$$

where  $K_s$  is the gain of the PWM driver,  $T_s$  is time constant, and  $s$  is differential operator.

The control voltage is transformed to the current of the VCM through current loop, and its control diagram is shown in Figure 7, where  $U_c$  is the input control voltage,  $G_c(s)$  is the transfer function of current loop PID controller,  $1/K_i$  is the current conversion factor,  $U_m$  is the operating voltage of VCM coil,  $U_B$  is the back electromotive force of the VCM coil,  $G_{LR}(s)$  is the equivalent transfer function of the VCM, and  $I_m$  is the current of VCM coil.



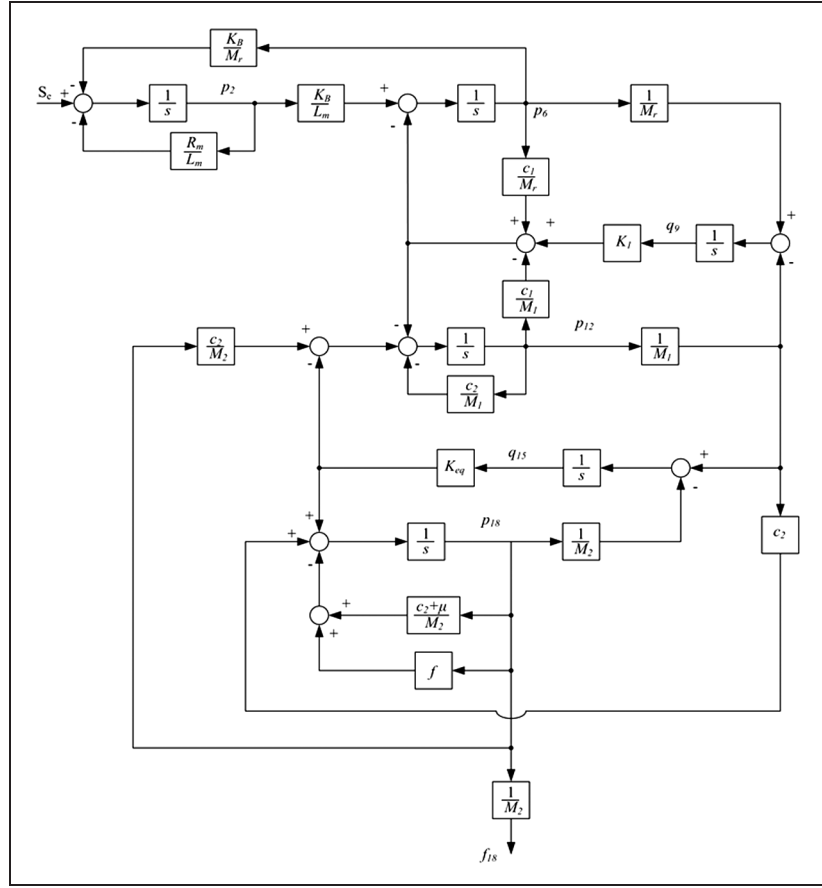


Figure 5. The global system control diagram for the Y-axis servomechanism.

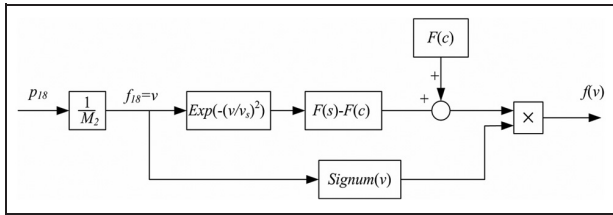


Figure 6. The control diagram for Y-axis nonlinear friction.

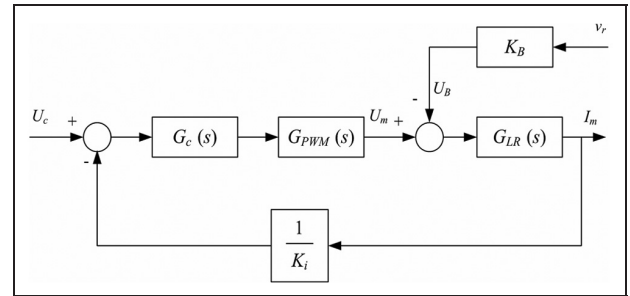


Figure 7. The current loop control diagram of the controller.

The inertia force and friction are compensated in the current loop, and the control diagram is displayed in Figure 8, where  $a_r$  is the acceleration of VCM coil,  $G_a(s)$  and  $G_f(s)$  are the transfer functions of the inertia force and friction compensators,  $G_a(s) = K_a$ ,  $G_f(s) = K_f$ ,  $K_a$  and  $K_f$  are constants,  $U_a$  and  $U_f$  are the control voltages of the inertia force and friction compensators, respectively. Thus the following equations can be obtained.

$$U_a = a_r \cdot G_a(s) = a_r \cdot K_a = (K_a \cdot F_{i1})/M_r \quad (21)$$

$$U_f = \text{signum}(v_r) \cdot G_f(s) = \text{signum}(v_r) \cdot K_f \quad (22)$$

$$U_m = I_m/K_i = F_m/(K_i \cdot K_f) \quad (23)$$

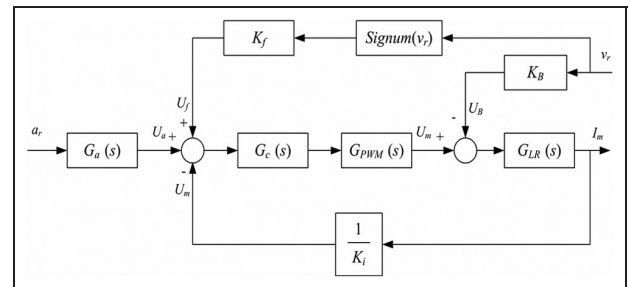


Figure 8. The control diagram for inertia force and friction compensations.



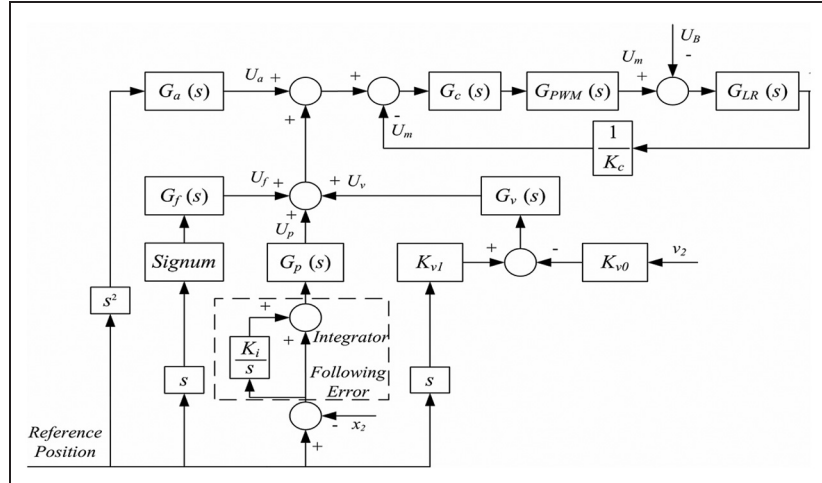


Figure 11. The control diagram for the X-axis force compensation.

Taking the motion parameters of X-axis VCM coil as the reference commands, the control diagram for X-axis force compensation is obtained, and it is depicted in Figure 11. The integral of displacement following error is used to eliminate the position steady error. The response stiffness of the servomechanism is determined by the performance of the spring-force compensator. The damping characteristics of the servomechanism are determined by the performance of the damping-force compensator, and the displacement following error related to the speed can be eliminated, meanwhile the overshoot is reduced by increasing the gain of the compensator. The displacement following error related to the acceleration can be eliminated by the inertia force compensator, and the frictional effect can be reduced by the friction compensator.

The main parameters of the controller are determined by

$$K_a = M_r / (K_i \cdot K_f) \quad (27)$$

$$K_F = F_c / (K_i \cdot K_f) \quad (28)$$

$$K_v \cdot K_{v0} = C_1 / (K_i \cdot K_f) \quad (29)$$

$$K_p = K_1 / (K_i \cdot K_f) \quad (30)$$

The Y-axis controller design process is similar to the X-axis. According to the bond graph of Y-axis servomechanism, the following equation can be obtained.

$$F_L = F_{ily} + F_{dy} + F_{sy} + F_{F1y} \quad (31)$$

Thus

$$F_L = M_r a_r + C_2(v_r - v_2) + K_{eq}(y_1 - y_2) + \mu v_r \quad (32)$$

Based on the principle of force compensator, the following equations can be got.

$$U_a = a_r \cdot G_a(s) = a_r \cdot K_a \quad (33)$$

$$U_f = \text{signum}(v_r) \cdot G_f(s) = \text{signum}(v_r) \cdot K_F \quad (34)$$

$$U_v = G_v(s) \cdot (K_{v1}v_r - K_{v0}v_2) \quad (35)$$

$$U_p = G_p(s) \cdot (y_r - y_2) = K_p \cdot (y_r - y_2) \quad (36)$$

The main parameters of Y-axis controller can be calculated by equations (27)–(30).

Simulations are carried out using MATLAB/SIMULINK software to investigate the performance of the controllers. For X-axis controller,  $K_a = 0.5$ ,  $K_F = 5$ ,  $K_v = 2$  and  $K_p = 21$ , and for Y-axis controller,  $K_a = 0.6$ ,  $K_F = 9$ ,  $K_v = 3$  and  $K_p = 15$ . The reference displacement is defined as 2 mm and the simulation results of step responses are shown in Figure 12. It can be seen that the X-axis settling time of the motion is 63 ms, the overshoot is 1.1%, and the steady-state error of displacement is  $\pm 1.5 \mu\text{m}$ . The Y-axis settling time of the motion is 65 ms, the overshoot is 0.5%, and the steady-state error of displacement is  $\pm 1.5 \mu\text{m}$ .

## Experiments

Experiments are carried out to examine the performance of the XY stage, and the experimental setup is shown in Figure 13. SMAC LAL300 VCMs are adopted as the drivers of the XY stage. The RENISHAW RGH22 linear grating encoders are used as the feedback sensors for X- and Y-axes tables. The implementation of the controller is realized through Turbo PMAC2 PCI motion control card. A RENISHAW EC10/ML10 laser interferometer is utilized to investigate the characteristics of the stage. To reduce the influences caused by the vibration and noise from the ground surface, the system is placed on a Newport RS-4000 vibration isolating table with air bearings.

Figure 14 provides the step responses of X-axis and Y-axis tables. Based on the simulation parameter values of the controller, the actual parameter tuning are carried out. There are only four parameters to be tuned, and the control algorithm is simple, thus reducing the calculation cost. Finally the parameter values are determined. For the X-axis controller,  $K_a = 0.6$ ,  $K_F = 7$ ,  $K_v = 5$  and  $K_p = 16$ , and for the Y-axis controller,  $K_a = 0.8$ ,  $K_F = 8$ ,  $K_v = 5$  and  $K_p = 12$ . The  $\pm 1.5 \mu\text{m}$  band at the desired level is used as the acceptable



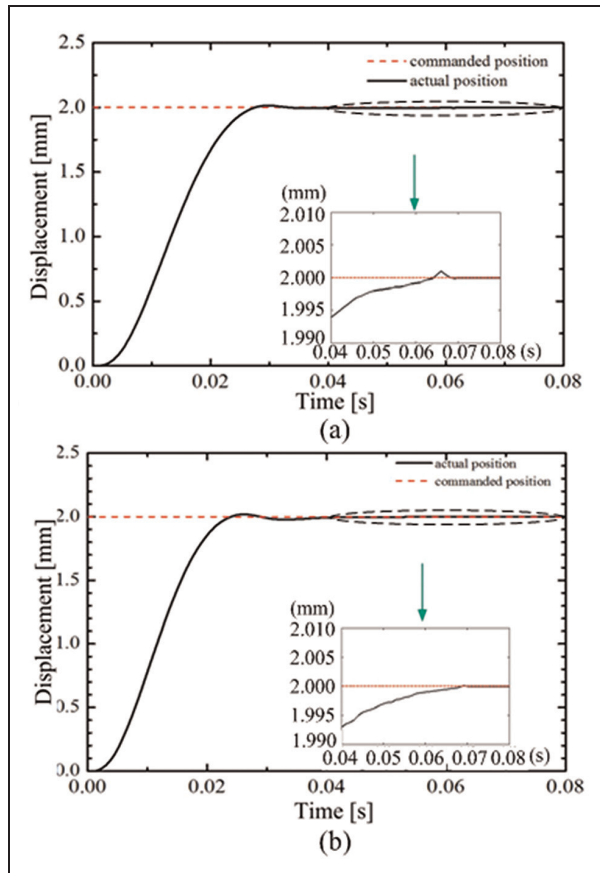


**Figure 12.** Simulation results for the motion of the XY stage: (a) for the X-axis, and (b) for the Y-axis.

range of variation from the desired response, and thus the X-axis table settling time is found to be 64 ms, the overshoot is 0.7%. Y-axis table settling time is 62 ms, and the overshoot is 0.8%.

The parabola velocity response curves are shown in Figure 15. It can be concluded that the actual position curves can match well with the command positions. The X-axis dynamic position tracking errors are within  $\pm 2.5 \mu\text{m}$  and the Y-axis dynamic position tracking errors are within  $\pm 4 \mu\text{m}$ . The simulation results are in a good agreement with the experimental results, which proves the correctness of the theoretical model.

For the positioning accuracy and repeated positioning accuracy, the ISO standard for the XY stage of machine tools is adopted, it is measured using the RENISHAW laser interferometer, and then the data is processed using RENISHAW software. Motion range of 12 mm is divided into six segments by seven points. When the table moves with the step size of 2 mm, laser interferometer measures the displacement errors of the seven points, and five motion cycles are operated, and thus 10 displacement errors are recorded in all at every point. Thus, the positioning accuracy and repeatability of the X-axis and Y-axis can be obtained using the recorded data. The recorded data are plotted in Figure 16. Forward stroke displacement error curve is expressed by continuous line, and backward stroke displacement error curve is described by dashed line. The results indicate that X-axis positioning

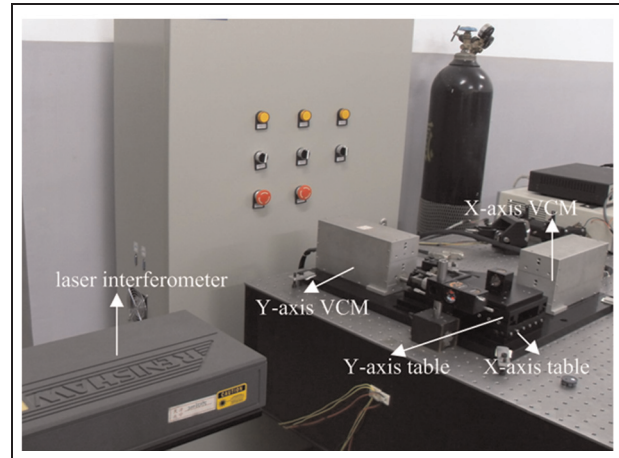


**Figure 13.** The experimental setup.

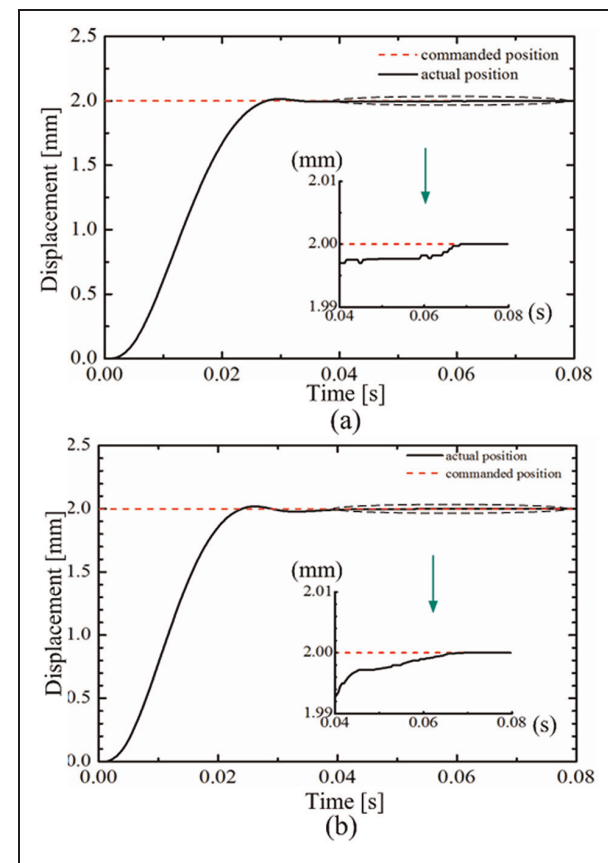


**Figure 14.** The step responses of the XY stage: (a) for the X-axis, and (b) for the Y-axis.

accuracy is  $1.75 \mu\text{m}$ , and the repeatability is  $0.9 \mu\text{m}$ . Y-axis positioning accuracy and repeatability are  $1.5 \mu\text{m}$  and  $0.8 \mu\text{m}$ , respectively.

The X- and Y-axes positioning accuracy has been simultaneously measured across the entire workspace, and the X-and

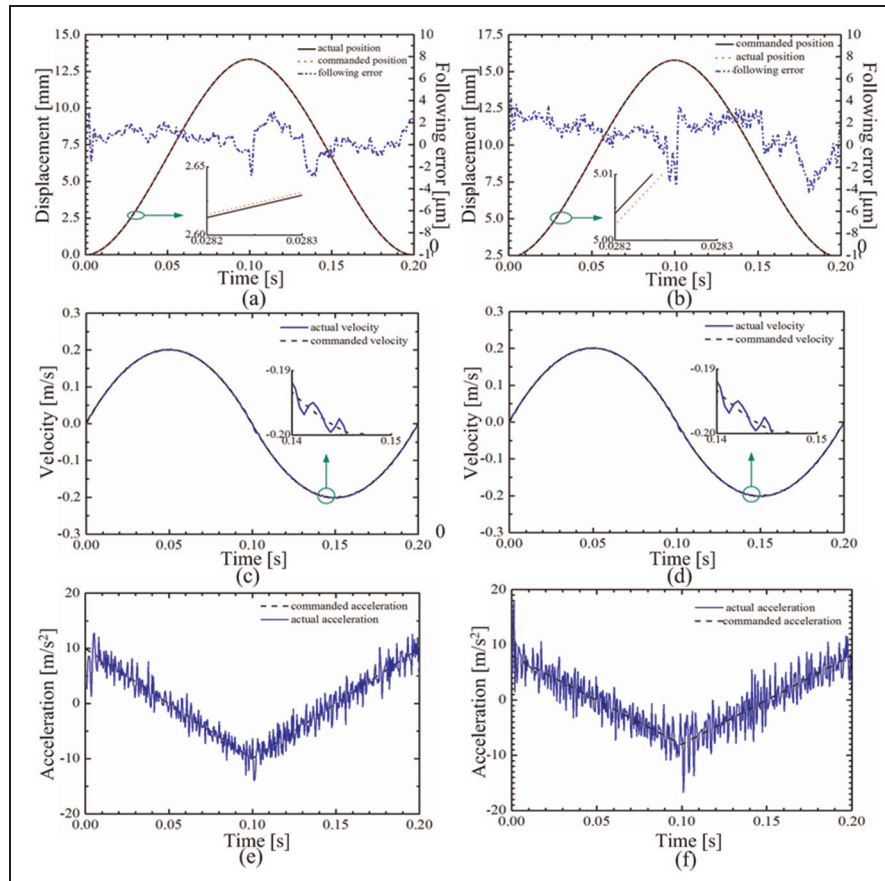


**Figure 15.** The parabola velocity response curves: (a) X-axis displacement, (b) Y-axis displacement, (c) X-axis velocity, (d) Y-axis velocity, (e) X-axis acceleration, and (f) Y-axis acceleration.

**Table 1.** The main performance indexes of the XY stage.

|        | Repeating positioning accuracy<br>( $\mu\text{m}$ ) | Maximum speed<br>(m/s) | Resolution<br>( $\mu\text{m}$ ) | Motion stroke<br>(mm) |
|--------|---|------------------------|---------------------------------|-----------------------|
| X axis | 0.95  | 0.45                   | 0.5                             | 50                    |
| Y axis | 0.9   | 0.62                   | 0.5                             | 50                    |

Y-axes linear encoders have been used to record the actual positions. The results show that X-axis positioning accuracy is  $1.85 \mu\text{m}$ , and the repeatability is  $0.95 \mu\text{m}$ . Y-axis positioning accuracy and repeatability are  $1.75 \mu\text{m}$  and  $0.9 \mu\text{m}$ , respectively.

The main performance indexes of the XY stage are tested and summarized in Table 1.

2-DOF trajectory tracking experiments have also been performed to investigate the tracking performance of the XY stage, and the dynamic tracking errors of all the points is used to describe the trajectory tracking performance of the XY stage. Figure 17 plots the tracking results of the linear trajectory with an obliquity of  $45^\circ$ . From Figure 17, it is seen that the actual trajectory almost coincides with the desired trajectory, and there is a little delay of Y-axis motion compared

with X-axis motion in the positive motion, while in the negative motion, there is a little delay of X-axis motion compared with Y-axis motion.

Planar circular trajectories are also chosen as the desired trajectories, and the displacements of the stage with different displacement commands are plotted in Figure 18, where the diameters of the two command circles are 16 mm and 4 mm, respectively. It is known from Figure 18 that the actual trajectories can track the desired circular trajectories well, and the result shows that the X-axis dynamic position tracking errors are within  $\pm 2.5 \mu\text{m}$  and the Y-axis dynamic position tracking errors are within  $\pm 3.0 \mu\text{m}$ .

The capability of tracking more complex trajectory is further examined, and the following smooth trajectory is chosen as the reference trajectory.

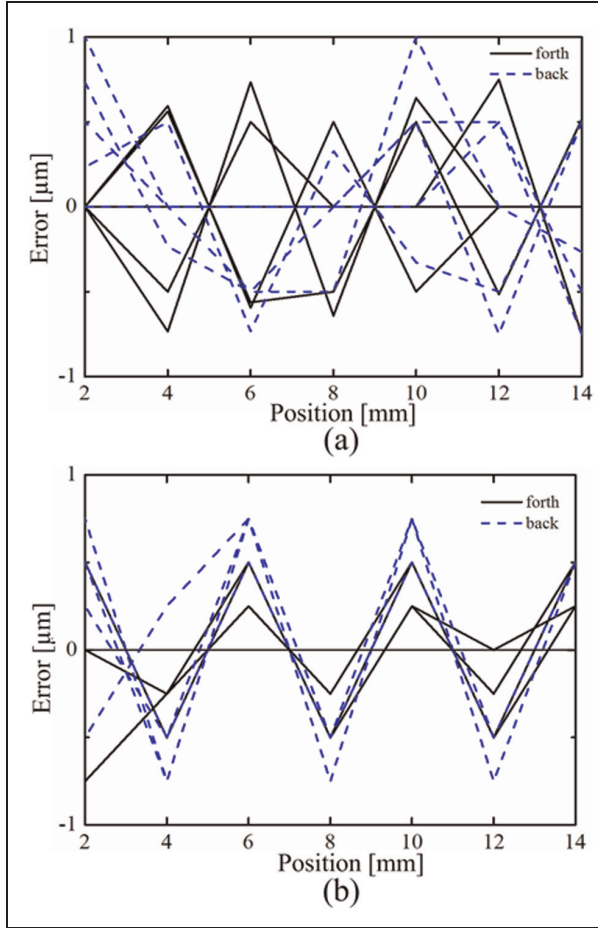


**Figure 16.** The positioning accuracy and repeatability: (a) for the X-axis; and (b) for the Y-axis.

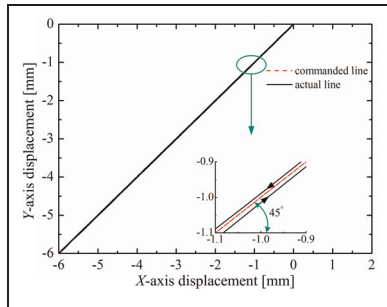


**Figure 17.** The tracking results of the linear trajectory.

$$\begin{aligned} x_r &= 4 \sin(\pi t - 0.5\pi) + 2 \sin(8\pi t - 0.5\pi) \\ y_r &= 4 \sin(\pi t) + 2 \sin(8\pi t) \end{aligned} \quad (37)$$

where  $x_r$ ,  $y_r$  are the X- and Y-axes command displacements, respectively, and  $t$  is time.

The trajectory tracking result is displayed in Figure 19, which shows that the stage can track the smooth trajectory well. During the motion process, the X-axis dynamic position tracking errors are within  $\pm 2.5\mu\text{m}$  and the Y-axis dynamic position tracking errors are within  $\pm 3.5\mu\text{m}$ .

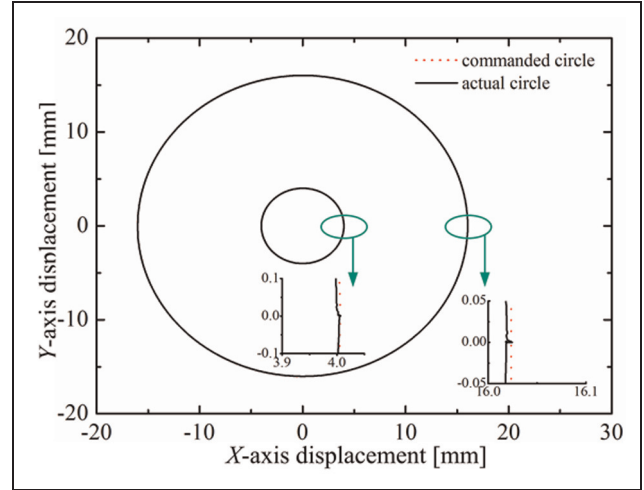


**Figure 18.** The tracking results of different reference circular trajectory.

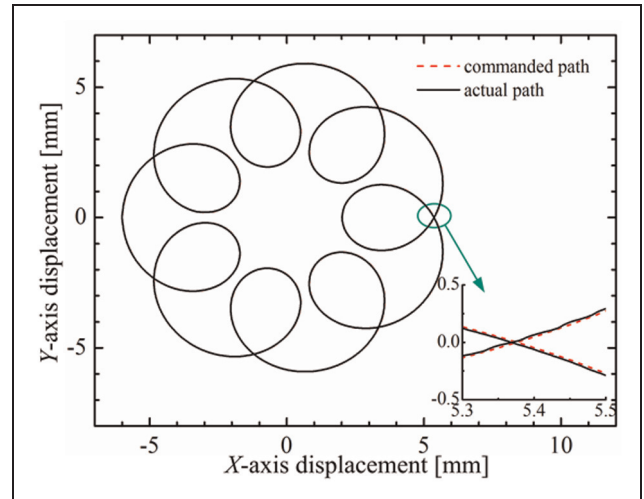


**Figure 19.** The trajectory tracking of the smooth trajectory.

## Conclusions

To improve the quality and efficiency of semiconductor packaging, the dynamic modeling, controller design and experimental tests of a LVCM direct-drive XY positioning stage are carried out in this paper. Based on the characteristics of the servomechanisms of the XY stage, the bond graphs of the stage are established, and the state space equations are obtained. The controller based on force compensations is proposed to control the XY stage, and it is realized through transforming the forces that applied to the VCM coil and tables to the control voltage signals. The performance of the XY stage are evaluated by experimental tests. The results show that when the reference displacements are defined as 2 mm, the settling time of the X-axis movement is 64 ms, and the overshoot is 0.7%. Y-axis settling time is 62 ms, and the overshoot is 0.8%. X-axis positioning accuracy is  $1.85\mu\text{m}$ ,

and the repeatability is  $0.95\ \mu\text{m}$ .  $Y$ -axis positioning accuracy and repeatability are  $1.75\ \mu\text{m}$  and  $0.9\ \mu\text{m}$ , respectively. The linear, circular and complex curve trajectory experimental results indicate the trajectory tracking performance of the  $XY$  stage are very well.

### Conflict of interest

The authors declare that there is no conflict of interest.

### Funding

The support of this work by the National Natural Science Foundation of China (grant numbers 51205279 and 51175372), the Science and Technology Commission of Tianjin Municipality (grant number 13JCQNJC04100), the Tianjin University for Peiyang Elite Scholar (grant number 60301014) and CSC Scholarship are gratefully acknowledged.

### Notation

|             |  |
|-------------|--|
| $a_r$       | acceleration of VCM coil                                       |
| $C$         | capacitor element  |
| $C_1$       | damping between coil and the guiding fin                       |
| $C_2$       | equivalent damping between the $Y$ -axis guiding fin and table |
| $e$         | effort   |
| $f$         | flow   |
| $F$         | force generated by the VCM                                     |
| $F_c$       | coulomb friction   |
| $F_d$       | damping force  |
| $F_{dy}$    | $Y$ -axis damping force  |
| $F_{F1}$    | friction of the $X$ -axis coil                                 |
| $F_{F1y}$   | friction of the $Y$ -axis coil                                 |
| $F_{F2}$    | friction of the $X$ -axis table                                |
| $F_{F2y}$   | friction of the $Y$ -axis table                                |
| $F_{i1}$    | inertia force of the $X$ -axis coil                            |
| $F_{i1y}$   | inertia force of the $Y$ -axis coil                            |
| $F_{i2}$    | inertia force of the $X$ -axis table                           |
| $F_{i2y}$   | inertia force of the $Y$ -axis table                           |
| $F_L$       | output force of the coil                                       |
| $F_s$       | equivalent spring force  |
| $F_{st}$    | static friction  |
| $F_{sy}$    | $Y$ -axis equivalent spring force                              |
| $G_a(s)$    | transfer function of the inertia force                         |
| $G_c(s)$    | transfer function of current loop PID controller               |
| $G_f(s)$    | transfer function of friction compensator                      |
| $G_v(s)$    | transfer function of damping force compensator                 |
| $G_p(s)$    | transfer function of spring force compensator                  |
| $G_{LR}(s)$ | equivalent transfer function of the VCM                        |
| $i$         | current intensity through the coil                             |
| $I_m$       | current of VCM coil  |
| $K$         | stiffness of the preload spring                                |
| $K_1$       | connecting stiffness between coil and the guiding fin          |
| $K_c$       | contact stiffness between the bearing and the lapping plate    |

|          |  |
|----------|--|
| $1/K_i$  | current conversion factor                    |
| $K_s$    | gain of the PWM driver                       |
| $K_t$    | stiffness of the flexure hinge               |
| $K_{v0}$ | velocity feedback coefficient                |
| $K_{v1}$ | velocity gain of VCM coil                    |
| $K_B$    | coefficient of induced electromotive force   |
| $K_F$    | force coefficient                            |
| $L_m$    | inductance of the VCM coil                   |
| $M_1$    | equivalent mass of the $Y$ -axis guiding fin |
| $M_2$    | equivalent mass of the $Y$ -axis table       |
| $M_3$    | mass of the $X$ -axis table                  |
| $M_r$    | mass of the coil                             |
| $p(t)$   | time integral of effort                      |
| $q(t)$   | time integral of flow                        |
| $R$      | resistor elements                            |
| $R_m$    | resistance of the VCM coil                   |
| $s$      | differential operator                        |
| $S_e$    | effort source                                |
| $T_s$    | time constant                                |
| $u_x$    | input variable                               |
| $U$      | voltage applied to the VCM                   |
| $U_a$    | control voltage of the inertia force         |
| $U_c$    | input control voltage                        |
| $U_f$    | control voltage of friction compensator      |
| $U_B$    | back electromotive force of the VCM coil     |
| $U_m$    | operating voltage of VCM coil                |
| $v$      | motion velocity of the VCM coil              |
| $v_2$    | velocity feedback                            |
| $v_f$    | velocity                                     |
| $v_s$    | Stribeck velocity                            |
| $x$      | displacement of $X$ -axis table              |
| $x_1$    | displacement of $X$ -axis VCM coil           |
| $x_2$    | displacement of table                        |
| $y_1$    | displacement of $Y$ -axis guiding fin        |
| $y_2$    | displacement of $Y$ -axis table              |
| $y_x$    | output variable                              |
| $\mu$    | viscous friction coefficient                 |

### References

- Adamy J and Flemming A (2004) Soft variable-structure controls: A survey. *Automatica* 40: 1821–1844.
- Aized T and Shirinzadeh B (2011) Robotic fiber placement process analysis and optimization using response surface method. *Int J Adv Manuf Technol* 55: 393–404.
- Ang KH, Chong G and Li Y (2005) PID control system analysis, design, and technology. *IEEE Trans Control Syst Technol* 13: 559–576.
- Cai T, Zhang M, Zhu Y and Hu C (2011) Dynamic modeling and analysis of a 3-DOF ultra-precision positioning stage with air bearing. *Procedia Eng* 16: 264–270.
- Dejima S, Gao W, Katakura K, et al. (2005) Dynamic modeling, controller design and experimental validation of a planar motion stage for precision positioning. *Precis Eng* 29: 263–271.
- Fatikow S, Eichhorn V, Stolle C, et al. (2008). Development and control of a versatile nanohandling robot cell. *Mechatronics* 18(7): 370–80.
- Ferreira PM, Qing Y and Dong J (2007) Design, analysis, fabrication and testing of a parallel-kinematic micropositioning  $XY$  stage. *Int J Mach Tools Manuf* 47: 946–961.
- Fung R-F, Hsu Y-L and Huang M-S (2009) System identification of a dual-stage  $XY$  precision positioning table. *Precis Eng* 33: 71–80.



- Hace A, Jezernik K, Curk B and Terbuc M (1998) Robust motion control of *XY* table for laser cutting machine. *Proceedings of the 1998 24th Annual Conference of the IEEE Industrial Electronics Society*, Aachen, Germany, pp. 1097–1102.
- Hwang J, Park C-H and Kim S-W (2010) Estimation method for errors of an aerostatic planar *XY* stage based on measured profiles errors. *Int J Adv Manuf Technol* 46: 877–883.
- Khan MU, Bencheikh N, Prella C, et al. (2012) A long stroke electromagnetic *XY* positioning stage for micro applications. *IEEE ASME Trans Mechatron* 17(5): 866–875.
- Li YM and Xu QS (2011). A novel piezoactuated *XY* stage with parallel, decoupled, and stacked flexure structure for micro-/nanopositioning. *IEEE Trans Ind Electron* 58: 3601–3615.
- Liang Q, Zhang D, Song Q and Ge Y (2010) Design of a compliant *XY* stage with embedded force sensor for micro-scale positioning. *Proceedings of 2010 IEEE International Conference on Information and Automation*, Harbin, China, pp. 1494–1499.
- Liaw HC, Shirinzadeh B and Smith J (2008) A robust motion tracking control of piezo-driven flexure-based four-bar mechanism for micro/nano manipulation. *Mechatronics* 18(2): 111–120.
- Liu ZZ, Luo FL and Rahman MA (2005) Robust and precision motion control system of linear-motor direct drive for high-speed X-Y table positioning mechanism. *IEEE Trans Ind Electron* 52: 1357–1363.
- Liu ZZ, Luo FL and Rashid MH (2003) QFT-based robust and precision motion control system for a high speed direct-drive *XY* table positioning mechanism. *Proceedings of the IEEE Industry Applications Conference*, UT, pp. 293–300.
- Mou S-C and Sung C-H (2012) Fuzzy positioning control of the novel single-axis piezoelectric actuated stage. *Proceedings of 2012 International Symposium on Computer, Consumer and Control*, Taichung, Taiwan, pp. 771–776.
- Sanchez-Salmeron AJ and Ricolfe-Viala C (2012) A flexible packaging station for micro-bulk-forming applications based on a standard carrier. *Int J Adv Manuf Technol* 61: 529–536.
- Sun L, Li T and Liu Y (2011) Modeling and analysis of a high acceleration and precision linear motor direct drive motion stage with bond graph approach. *Robot* 33: 467–474.
- Teo CS, Tan KK, Lim SY, et al. (2007) Dynamic modeling and adaptive control of a H-type gantry stage. *Mechatronics* 17: 361–367.
- Tian Y, Shirinzadeh B and Zhang D (2009) A flexure-based mechanism and control methodology for ultra-precision turning operation. *Precis Eng* 33: 160–166.
- Tomizuka M (1987) Zero phase error tracking algorithm for digital control. *J Dyn Syst Meas Control Trans ASME* 109: 65–68.
- Wang F, Li J, Liu S, et al. (2014) An improved adaptive genetic algorithm for image segmentation and vision alignment used in micro-electronic bonding. *IEEE/ASME Transactions on Mechatronics* 19(3): 916–923.
- Wang F, Zhao X, Zhang D, et al. (2011) Robust and precision motion control for a directly driven *XY* table. *Proceedings of IMechE, Part C, Journal of Mechanical Engineering Science* 225(5): 1107–1120.
- Wang F, Zhao X, Zhang D and Wu Y (2009a) Development of novel ultrasonic transducers for microelectronics packaging. *Journal of Materials Processing Technology* 209(3): 1291–1301.
- Wang W, Shin D, Han C and Choi H (2009b) Modeling and simulation for dual stage system using bond graph theory. *Proceedings of International Symposium on Optomechatronic Technologies*, Istanbul, Turkey, pp. 197–202.
- Wang Y, Xiong ZH and Ding H (2006) Robust controller based on friction compensation and disturbance observer for a motion platform driven by a linear motor. *Proc IMechE Part I: J Syst Control Eng* 220: 33–39.
- Wu YT and Ding H (2007) Reference adjustment for a high-acceleration and high-precision platform via A-type of iterative learning control. *Proc IMechE Part I: J Syst Control Eng* 221:781–789.
- Xu L and Yao B (2000) Coordinated adaptive robust contour tracking of linear-motor-driven tables in task space. *Proceedings of the IEEE Conference on Decision and Control*, Sydney, Australia, pp. 2430–2435.
- Xu QS and Li YM (2009) Radial basis function neural network control of an *XY* micropositioning stage without exact dynamic model. *Proceedings of 2009 IEEE/ASME International Conference on Advanced Intelligent Mechatronics*, Singapore, pp. 498–503.
- Zhang H, Wang F, Zhao X, et al. (2013) Electrical matching of a piezoelectric ultrasonic transducer for microelectronic bonding. *Sensors and Actuators A: Physical* 199(1): 241–249.
- Zhao Y, Yang K, Zhu Y and Pan S (2010) Modeling and analyzing of an H-drive precision *XY* stage. *Proceedings of 2010 International Conference on Mechanic Automation and Control Engineering*, Wuhan, China, pp. 6311–6314.